

Swift observations of two supergiant fast X-ray transient prototypes in outburst

R. Farinelli^{1,2}, P. Romano², V. Mangano², C. Ceccobello¹, L. Ducci³,
S. Vercellone², P. Esposito⁴, J.A. Kennea⁵, D.N. Burrows⁵

¹Dipartimento di Fisica, Università di Ferrara, via Saragat 1, 44122, Ferrara, Italy

²INAF, Istituto di Astrofisica Spaziale e Fisica Cosmica, via U. La Malfa 153, 90146 Palermo, Italy

³Institut für Astronomie und Astrophysik, Universität Tübingen, Sand 1, 72076 Tübingen, Germany

⁴INAF, Osservatorio Astronomico di Cagliari, località Poggio dei Pini, strada 54, 09012 Capoterra, Italy

⁵Department of Astronomy and Astrophysics, Pennsylvania State University, University Park, PA 16802, USA

Accepted 2012 May 30. Received 2012 May 30; in original form 2012 April 17

ABSTRACT

We report on the results from observations of the most recent outbursts of XTE J1739–302 and IGR J17544–2619, which are considered to be the prototypes of the supergiant fast X-ray transient (SFXT) class. They triggered the *Swift*/BAT on 2011 February 22 and March 24, respectively, and each time a prompt *Swift* slew allowed us to obtain the rich broad-band data we present. The XRT light curves show the descending portion of very bright flares that reached luminosities of $\sim 2 \times 10^{36}$ and $\sim 5 \times 10^{36}$ erg s^{−1}, respectively. The broad-band spectra, when fit with the usual phenomenological models adopted for accreting neutron stars, yield values of both high energy cut-off and e-folding energy consistent with those obtained from previously reported outbursts from these sources. In the context of more physical models, the spectra of both sources can be well fitted either with a two-blackbody model, or with a single unsaturated Comptonization model. In the latter case, the model can be either a classical static Comptonization model, such as COMPPT, or the recently developed COMPAG model, which includes thermal and bulk Comptonization for cylindrical accretion onto a magnetized neutron star. We discuss the possible accretion scenarios derived by the different models, and we also emphasize the fact that the electron density derived from the Comptonization models, in the regions where the X-ray spectrum presumably forms, is lower than that estimated using the continuity equation at the magnetospheric radius and the source X-ray luminosity, and we give some possible explanations.

Key words: X-rays: binaries – X-rays: individual: XTE J1739–302, IGR J17544–2619.
Facility: *Swift*

1 INTRODUCTION

Supergiant fast X-ray transients (SFXTs) are a class of High Mass X-ray Binaries (HMXBs) associated with OB supergiant stars. In the X-rays they display outbursts significantly shorter than those of typical Be/X-ray binaries characterized by bright flares with peak luminosities of 10^{36} – 10^{37} erg s^{−1} which last a few hours (as observed by *INTEGRAL*; Sguera et al. 2005; Neugeruela et al. 2006b). As their quiescence is characterized by a luminosity of $\sim 10^{32}$ erg s^{−1} (e.g. in’t Zand 2005; Bozzo et al. 2010), their dynamic range is of 3–5 orders of magnitude. While in outburst, their hard X-ray spectra resemble those of HMXBs hosting an accreting neutron star (NS), with hard power laws below 10 keV with high energy cut-offs at ~ 15 –30 keV. So, even if pulse periods have only been measured for a few SFXTs, it is tempting to assume that all SFXTs might host a NS.

The physical context originating the outbursts has been claimed to be related either to the properties of the wind from the supergiant companion (in’t Zand 2005; Walter & Zurita Heras 2007; Neugeruela et al. 2008; Sidoli et al. 2007) or to the presence of a centrifugal or magnetic barrier (Grebenev & Sunyaev 2007; Bozzo et al. 2008).

XTE J1739–302 was discovered by *RXTE* in August 1997 (Smith et al. 1998), when it reached a peak flux of 3.6×10^{-9} erg cm^{−2} s^{−1} (2–25 keV). It has a long history of flaring recorded by *INTEGRAL* (Sguera et al. 2006; Walter & Zurita Heras 2007; Blay et al. 2008) and by *Swift* (Sidoli et al. 2009b,a; Romano et al. 2011c,b). Recently, Drave et al. (2010) reported the discovery of a 51.47 ± 0.02 d orbital period based on ~ 12.4 Ms of *INTE-*

Table 1. Log of the observations of XTE J1739–302 and IGR J17544–2619 with *Swift*.

Source	Sequence	Instrument /Mode	Start time (UT) (yyyy-mm-dd hh:mm:ss)	End time (UT) (yyyy-mm-dd hh:mm:ss)	Exposure (s)	Time Since Trigger (s)
XTE J1739–302	00446475000	BAT/evt	2011-02-22 07:19:44	2011-02-22 07:36:46	1022	-119
	00446475000	XRT/WT	2011-02-22 07:24:10	2011-02-22 09:04:37	1271	147
	00446475000	XRT/PC	2011-02-22 09:04:39	2011-02-22 09:13:55	554	6176
IGR J17544–2619	00449907000	BAT/evt	2011-03-24 01:53:04	2011-03-24 02:13:06	1202	-239
	00449907000	XRT/WT	2011-03-24 01:59:15	2011-03-24 03:18:22	657	133
	00449907000	XRT/PC	2011-03-24 02:10:07	2011-03-24 04:01:03	3360	784
	00035056150	XRT/PC	2011-03-27 19:54:23	2011-03-27 20:11:56	1046	323840
	00035056151	XRT/PC	2011-03-28 20:10:36	2011-03-28 20:21:58	662	411213
	00035056152	XRT/PC	2011-03-29 20:15:13	2011-03-29 20:23:57	504	497890

GRAL data¹. The optical counterpart is an O8I ab star at 2.7 kpc (Negueruela et al. 2006a; Rahoui et al. 2008).

IGR J17544–2619 was first detected by *INTEGRAL* in 2003 (Sunyaev et al. 2003), when the source reached a flux of 160 mCrab (18–25 keV). Several more flares, lasting up to 10 hours, were detected by *INTEGRAL* in the following years (Grebenev et al. 2003, 2004; Sguera et al. 2006; Walter & Zurita Heras 2007; Kuulkers et al. 2007) with fluxes up to 400 mCrab (20–40 keV); some were also found in archival *BeppoSAX* observations (in’t Zand et al. 2004). Subsequent flares were observed by *Swift* (Krimm et al. 2007; Sidoli et al. 2009b,a; Romano et al. 2011c,d,a), and *Suzaku* (Rampy et al. 2009). Clark et al. (2009) reported the discovery of a 4.926 ± 0.001 d orbital period based on ~ 4.5 years of *INTEGRAL* data. Recently, Drave et al. (2012) detected a transient 71.49 ± 0.02 s signal in RXTE observations from the region of IGR J17544–2619, which, if interpreted as the spin period of the NS in the system, places the source in the locus of the Corbet diagram (Corbet 1986) where classical wind-fed supergiant X-ray binaries can be found. The optical counterpart is an O9Ib star at 3.6 kpc (Pellizza et al. 2006; Rahoui et al. 2008).

XTE J1739–302 and IGR J17544–2619 are considered the prototypes of the SFXT class, and were extensively studied with *Swift*. In particular, in addition to the Burst Alert Telescope (BAT, Barthelmy et al. 2005) outburst detections and intensive X-ray Telescope (XRT, Burrows et al. 2005) follow-up, *Swift* has been studying their long-term properties (Romano et al. 2011c, and references therein). In this paper we examine the most recent outbursts of these two sources, which triggered the BAT in 2011. In particular, we apply, for the first time to SFXTs, the new COMPAG model by Farinelli et al. (2012, hereafter F12).

2 OBSERVATIONS AND DATA REDUCTION

XTE J1739–302 triggered the BAT on 2011 February 22 at 07:21:37 UT (image trigger=446475, Romano et al. 2011b). *Swift* immediately slewed to the target, so that the narrow-field instruments (NFI) started observing about 141 s after the trigger. After the initial automated target (AT) observation (two orbits for a total of ~ 1.8 ks net exposure spanning ~ 6.7 ks) no further NFI observations were performed.

¹ We note, however, that Romano et al. (2009) derived a marginal evidence, based on XRT data, of signal at $P_{\text{orb}} = 12.8658 \pm 0.0073$ d, or $1/4$ the period reported by Drave et al. (2010).

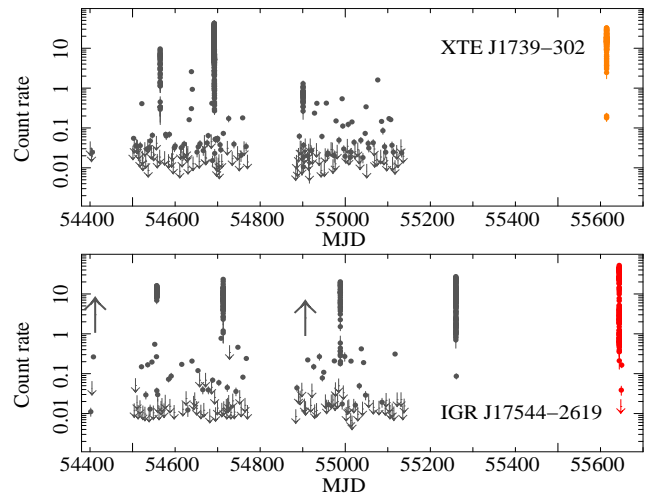


Figure 1. *Swift*/XRT (0.2–10 keV) long-term light curves of XTE J1739–302 and IGR J17544–2619. The downward-pointing arrows are 3σ upper limits. The upward-pointing arrows mark flares that triggered the BAT Transient Monitor on MJD 54414 and 54906. Data up to MJD ~ 55261 (grey) were published in Romano et al. (2009, 2011c,d).

IGR J17544–2619 (Romano et al. 2011a) triggered the BAT on 2011 March 24 at 01:56:57 UT (image trigger=449907, Romano et al. 2011a). *Swift* immediately slewed to the target, so that the NFIs started observing about 126 s after the trigger. The AT (sequence 00449907000) ran for two orbits, until ~ 7.4 ks after the trigger). Follow-up target of opportunity (ToO) observations for a total of 2.2 ks were obtained (sequences 00035056150–152) after the source emerged from Moon constraint. The data cover the first 6 d after the beginning of the outburst. Table 1 reports the log of the *Swift* observations used in this paper.

The BAT data were analysed using the standard BAT analysis software within FTOOLS in the HEASOFT package (v.6.11). Mask-tagged BAT light curves were created in the standard energy bands, and rebinned to fulfil at least one of the following conditions, achieving a signal-to-noise (S/N) of 5 or bin length of 10 s. Spectra were extracted from the whole event lists and within time intervals strictly simultaneous with the XRT. Response matrices were generated with BATDRMGEN using the latest spectral redistribution matrices. Survey data products, in the form of Detector

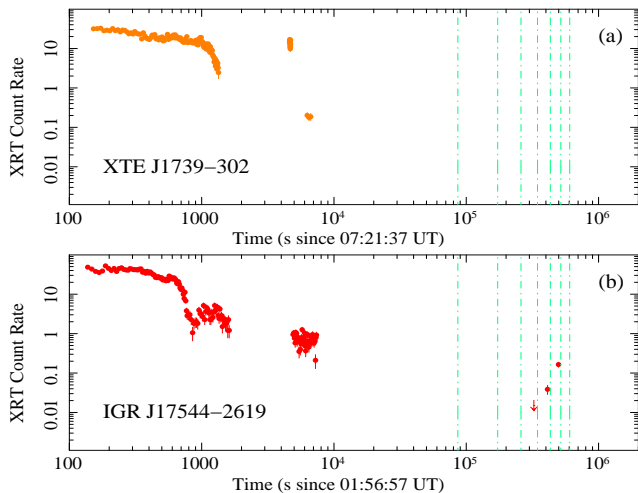


Figure 2. *Swift*/XRT (0.2–10 keV) light curves of the 2011 outbursts of XTE J1739–302 and IGR J17544–2619, as followed by *Swift*/XRT, referred to their respective BAT triggers (2011 February 22, 2011 March 24). Points denote detections, downward-pointing arrows 3σ upper limits. Where no data are plotted, no *Swift* data were collected. Vertical dashed lines mark time intervals equal to 1 day, up to a week.

Plane Histograms (DPH), are available, and were analysed with the standard BATSURVEY software.

The XRT data were processed with standard procedures (XRTPIPELINE v0.12.6), filtering and screening criteria by using FTOOLS. We considered both windowed-timing (WT) and photon-counting (PC) mode data, and selected event grades 0–2 and 0–12, for WT and PC data, respectively (Burrows et al. 2005). When appropriate, we corrected for pile-up by determining the size of the affected core of the point spread function (PSF) by comparing the observed and nominal PSF (Vaughan et al. 2006), and excluding from the analysis all the events that fell within that region. Background events were accumulated from source-free regions. For our timing analysis light curves were created for several values of signal-to-noise ratio (SNR) and number of counts per bin; all were corrected for PSF losses, vignetting and background. For our spectral analysis, we extracted events in the same regions as those adopted for the light curve creation; the data were rebinned with a minimum of 20–50 counts per energy bin, as appropriate, to allow χ^2 fitting, with the exception of low-count-statistics spectra, in which Cash (Cash 1979) statistics and spectra binned to 1 count per bin were used, instead. Ancillary response files were generated with XRTMKARF, to account for different extraction regions, vignetting, and PSF corrections. We used the latest spectral redistribution matrices in CALDB (20110915). For the luminosity calculation we adopted a distance of 2.7 kpc and 3.6 kpc for XTE J1739–302 and IGR J17544–2619, respectively (Rahoui et al. 2008).

All quoted uncertainties are given at 90% confidence level for one interesting parameter unless otherwise stated. The spectral indexes are parametrised as $F_\nu \propto \nu^{-\alpha}$, where F_ν ($\text{erg cm}^{-2} \text{s}^{-1} \text{Hz}^{-1}$) is the flux density as a function of frequency ν ; we adopt $\Gamma = \alpha + 1$ as the photon index, $N(E) \propto E^{-\Gamma}$ ($\text{ph cm}^{-2} \text{s}^{-1} \text{keV}^{-1}$).

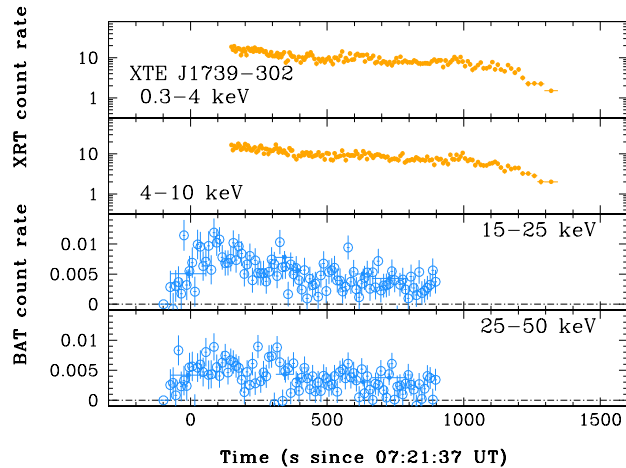


Figure 3. XRT and BAT light curves of the initial orbit of data of the 2011 February 22 outburst of XTE J1739–302 in units of count s^{-1} and $\text{count s}^{-1} \text{detector}^{-1}$, respectively. The empty circles correspond to BAT in event mode, filled circles to BAT survey mode data.

Table 2. Absorbed power-law spectral fits of XRT data of XTE J1739–302.

Spectrum ^a	N_{H}^b	Γ	Flux ^c	L^d	χ^2/dof C-stat (dof) ^e
WT (147–1343)	$2.35^{+0.15}_{-0.14}$	$0.79^{+0.06}_{-0.06}$	1.8	1.8	681/563
WT (4625–4697)	$3.18^{+0.78}_{-0.65}$	$1.13^{+0.29}_{-0.27}$	1.3	1.4	52/40
PC (6176–6730)	$6.44^{+4.69}_{-3.34}$	$1.42^{+1.18}_{-1.03}$	0.02	0.03	73.4(83)

^a Spectrum (seconds since trigger).

^b In units of 10^{22}cm^{-2} .

^c Observed 2–10 keV fluxes ($10^{-9} \text{erg cm}^{-2} \text{s}^{-1}$).

^d 2–10 keV luminosities in units of $10^{36} \text{erg s}^{-1}$, at 2.7 kpc.

^e Cash statistics (C-stat).

3 ANALYSIS AND RESULTS

Fig. 1 shows the *Swift*/XRT 0.2–10 keV light curve of XTE J1739–302 and IGR J17544–2619 throughout our 2007–2009 monitoring program (Romano et al. 2011c, and references therein) background-subtracted and corrected for pile-up, PSF losses, and vignetting. All data in one observation (1–2 ks) were generally grouped as one point, except for outbursts, which show up as a vertical lines on the adopted scale. The data already presented elsewhere are in grey. The details of the 2011 outbursts of XTE J1739–302 and IGR J17544–2619, referred to their respective BAT triggers, are shown in Fig. 2. In both cases the XRT caught the descending portion of a very bright flare in great detail. There is a similarity between the two outbursts, and also with previous outbursts of these sources [see figure 6 of Romano et al. (2011d), for a compendium of the best light curves collected before the currently presented ones and figure 9b–e of Sidoli et al. (2009a) for a comparison of different outbursts of the same source].

The details of the data selection and spectroscopic analysis on both sources are reported in the remainder of this Section. Here we summarise the models we adopted for the broad-band spectra. We first considered the phenomenological models typically used to de-

Table 3. Best-fit parameters of the phenomenological models for XTE J1739–302 and IGR J17544–2619 broad-band spectra, respectively. In the latter case an absorption edge was also included. CPL=cut-off powerlaw; HCP=powerlaw multiplied by exponential cut-off with e-folding factor.

Parameter	XTE J1739–302		IGR J17544–2619	
	CPL	HCP	CPL	HCP
$N_{\text{H}} (10^{22} \text{ cm}^{-2})$	$1.97^{+0.17}_{-0.16}$	$1.76^{+0.17}_{-0.15}$	$0.73^{+0.06}_{-0.06}$	$1.01^{+0.06}_{-0.05}$
$E_{\text{edge}} \text{ (keV)}$	–	–	$22.98^{+1.15}_{-1.12}$	–
τ_{edge}	–	–	$1.35^{+0.54}_{-0.43}$	–
Γ	$0.25^{+0.11}_{-0.10}$	$0.42^{+0.09}_{-0.09}$	$0.04^{+0.07}_{-0.07}$	$0.69^{+0.02}_{-0.04}$
$E_{\text{c}} \text{ (keV)}$	–	$9.56^{+0.99}_{-0.82}$	–	$5.66^{+0.54}_{-0.51}$
$E_{\text{f}} \text{ (keV)}$	$9.19^{+0.95}_{-0.80}$	$4.60^{+0.37}_{-0.36}$	$7.50^{+0.54}_{-0.49}$	$14.32^{+0.32}_{-1.61}$
$F_{2-10 \text{ keV}}^{\text{a}}$	2.4	2.3	3.1	3.2
$F_{1-100 \text{ keV}}^{\text{a}}$	7.0	7.1	7.6	9.0
$L_{2-10 \text{ keV}}^{\text{b}}$	2.0	2.0	4.8	5.0
$L_{1-100 \text{ keV}}^{\text{b}}$	6.1	6.1	11.9	14.1
χ^2/dof	364/243	336/242	344/296	324/297

^a Average observed flux in units of $10^{-9} \text{ erg cm}^{-2} \text{ s}^{-1}$.

^b In units of $10^{36} \text{ erg s}^{-1}$.

scribe the X–ray emission from accreting pulsars in HMXBs, i.e., *i*) simple absorbed (WABS in XSPEC) power laws; *ii*) absorbed power laws with exponential cut-offs (CUTOFFPL, hereon CPL); *iii*) absorbed power laws with high-energy cut-offs (HIGHECUT, hereon HCP). The simple advantage of this approach is that these fits yield easy-to-compare estimates of fluxes and luminosities. The disadvantage, however, is that little physical insight can be obtained from such fits, therefore we also considered the following physical models: *iv*) absorbed generic Comptonization models (COMPTT) in diffusion approximation for a disc geometry without a dynamical bulk component, *v*) a combination of two blackbodies (BB) with different temperatures and radii (BBODYRAD+BBODYRAD), sometimes used to fit the spectra of magnetars (Israel et al. 2008); *vi*) the new COMPMAG model, recently developed by F12. We refer the reader to that paper for a detailed description of the algorithm. Here we briefly remind the reader that COMPMAG is based on the solution of the radiative transfer equation for the case of cylindrical accretion onto the polar cap of a magnetized NS. The velocity field of the accreting matter can be increasing towards the NS surface, or it may be described by an approximate decelerating profile. In the former case, the free parameters are the terminal velocity at the NS surface, \bar{v} , and the index of the law $\beta(z) \propto z^{-\eta}$, while in the second case the law is given by $\beta(\tau) \propto -\tau$. The other free parameters of the model are the temperature of the BB seed photons, kT_{bb} , the electron temperature and vertical optical depth of the Comptonization plasma kT_{e} and τ , respectively, and the radius of the accretion column r_0 , in units of the NS Schwarzschild radius. The different combinations of these parameters determine the steepness of the spectrum at high energies and the rollover energy position.

However, given that the Comptonization spectra can be determined by only three quantities (slope, cut-off position and normalisation), for practical purposes it is generally not possible to keep free all the above mentioned parameters, a procedure which otherwise lead them to be completely unconstrained during the fitting procedure. In the following Sections we will report in more detail the procedure that we adopted in the spectral fitting.

3.1 XTE J1739–302

The XRT light curve (Fig. 2a) shows the descending part of a flare, that started off at a peak exceeding 30 counts s^{-1} then decreases to about $2.5 \text{ counts s}^{-1}$. A second flare is observed in the second orbit, with a count rate in the range $10\text{--}17 \text{ counts s}^{-1}$. In the third orbit the count rate was $\sim 0.2 \text{ counts s}^{-1}$. In Fig. 3 are reported the first orbit data of XTE J1739–302 in several energy bands. The event-by-event mask-weighted light curves only show the initial flare, which started at $\lesssim T - 70 \text{ s}$ with a slow rise, well defined in both soft bands. The source was still bright when the BAT event data end, at $T + 900 \text{ s}$. The BAT survey data cover the same timespan.

We extracted an XRT spectrum for each orbit of data as detailed in Table 2 and we fit them with an absorbed power-law model. The results are summarized in Table 2. By linking the N_{H} across the spectra, we can detect N_{H} variations, while the photon index is consistent with being constant, as previously reported in Sidoli et al. (2009b,a).

The BAT average spectrum ($T - 119$ to $T+903 \text{ s}$) can be fit by a simple power-law model with a photon index $\Gamma = 2.67^{+0.16}_{-0.15}$ ($F_{15-50 \text{ keV}} = 2.8 \times 10^{-9} \text{ erg cm}^{-2} \text{ s}^{-1}$); the fit, however, is not good ($\chi^2/\text{dof}=51/37$) and the residuals indicate that a curvature is present in the spectrum, which is best assessed in a broad-band analysis.

In order to perform broad-band spectroscopy of the outburst, we extracted strictly simultaneous spectra from the XRT and BAT event lists, i.e., in the time interval $147\text{--}903 \text{ s}$ since the BAT trigger (see Fig. 3). We fit them in the $0.5\text{--}10 \text{ keV}$ and $15\text{--}60 \text{ keV}$ energy bands for XRT and BAT, respectively. Factors were included in the fitting to allow for normalisation uncertainties between the two instruments, constrained within their usual ranges ($0.9\text{--}1.1$). A simple absorbed power-law model clearly yields an inadequate fit of the broad-band spectrum with a $\chi^2/\text{dof}=926/244$. A significant improvement is obtained when considering the other phenomenological curved models described above (see Table 3).

A more satisfactory fit is instead obtained with the model WABS×(BBODYRAD+BBODYRAD), whose results are reported in Table 4, while in Fig. 4 we show the deconvolved best-fit model and data.

We also tested the model WABS×COMPTT, which yields sta-

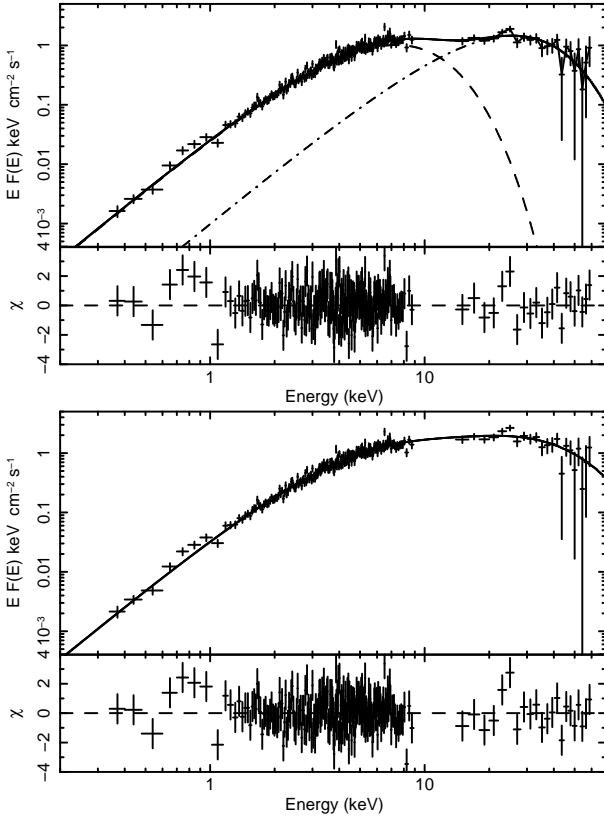


Figure 4. Absorption-corrected unfolded $EF(E)$ models and spectra, and residuals between the data and the model in units of σ for XTE J1739–302. *Upper panel:* BBODYRAD+BBODYRAD. *Lower panel:* COMPMAG.

Table 4. Best-fit parameters of the model WABS×(BBODYRAD+BBODYRAD) for XTE J1739–302 and IGR J17544–2619 broad-band spectra, respectively.

Parameter	XTE J1739–302	IGR J17544–2619
N_{H} (10^{22} cm $^{-2}$)	$1.07^{+0.09}_{-0.09}$	$0.58^{+0.07}_{-0.06}$
kT_{bb}^1 (keV)	$1.88^{+0.07}_{-0.06}$	$0.92^{+0.07}_{-0.07}$
$R_{\text{bb},1}$ (km)	$1.15^{+0.04}_{-0.05}$	$3.43^{+0.41}_{-0.34}$
kT_{bb}^2 (keV)	$6.62^{+0.49}_{-0.15}$	$3.45^{+0.08}_{-0.07}$
$R_{\text{bb},2}$ (km)	$0.11^{+0.01}_{-0.01}$	$0.77^{+0.04}_{-0.04}$
$F_{2-10 \text{ keV}}^a$	2.2	3.1
$F_{1-100 \text{ keV}}^a$	5.9	7.7
$L_{2-10 \text{ keV}}^b$	1.9	4.8
$L_{1-100 \text{ keV}}^b$	5.2	12.1
χ^2/dof	285/241	335/297

^a In units of 10^{-9} erg cm $^{-2}$ s $^{-1}$.

^b In units of 10^{36} erg s $^{-1}$.

tistically similar results, and we report the main values of the model in Table 5.

Finally, we tested the COMPMAG model assuming a free-fall like velocity profile ($\eta = 0.5$), two terminal velocities at the NS surface, $\varrho = 0.05$ and $\varrho = 0.2$, respectively, and NS albedo $A = 1$. The free parameters of the model during the fitting procedure were the seed BB temperature kT_{bb} , the electron temperature kT_e , and the vertical optical depth of the accretion column τ . We note that the latter quantity in this case is a factor about

Table 5. Best-fit parameters of the model WABS×COMPPT for XTE J1739–302 and IGR J17544–2619 broad-band spectra, respectively. As for the case of Table 3, an absorption edge was included in the model for IGR J17544–2619.

Parameter	XTE J1739–302	IGR J17544–2619
N_{H} (10^{22} cm $^{-2}$)	$0.81^{+0.11}_{-0.10}$	$0.58^{+0.07}_{-0.06}$
E_{edge} (keV)	–	$20.97^{+1.82}_{-1.23}$
τ_{edge}	–	$0.62^{+0.35}_{-0.31}$
kT_w (keV)	$1.34^{+0.07}_{-0.06}$	$0.63^{+0.07}_{-0.08}$
kT_e (keV)	$8.83^{+1.88}_{-1.11}$	$3.92^{+0.18}_{-0.16}$
τ	$3.61^{+0.51}_{-0.79}$	$10.67^{+0.71}_{-0.74}$
$F_{2-10 \text{ keV}}^a$	2.2	3.0
$F_{1-100 \text{ keV}}^a$	6.8	8.0
$L_{2-10 \text{ keV}}^b$	1.9	4.7
$L_{1-100 \text{ keV}}^b$	5.9	12.5
χ^2/dof	289/242	323/295

^a In units of 10^{-9} erg cm $^{-2}$ s $^{-1}$.

^b In units of 10^{36} erg s $^{-1}$.

Table 6. Best-fit parameters of the model WABS×COMPMAG for XTE J1739–302 and IGR J17544–2619 broad-band spectra, respectively. In both cases the fixed parameters are $\eta = 0.5$, $\varrho = 0.05$, $r_0 = 0.25$, and $A = 1$. Also in this case, as in Table 3, an absorption edge was included in the model for IGR J17544–2619.

Parameter	XTE J1739–302	IGR J17544–2619
N_{H} (10^{22} cm $^{-2}$)	$1.18^{+0.12}_{-0.09}$	$0.68^{+0.10}_{-0.08}$
E_{edge} (keV)	–	$21.71^{+1.84}_{-0.95}$
τ_{edge}	–	$0.81^{+0.52}_{-0.23}$
kT_{bb} (keV)	$1.63^{+0.10}_{-0.17}$	$0.73^{+0.11}_{-0.10}$
kT_e (keV)	$9.62^{+4.05}_{-2.57}$	$3.47^{+0.34}_{-0.02}$
τ	$0.33^{+0.30}_{-0.03}$	$1.19^{+0.09}_{-0.10}$
$F_{2-10 \text{ keV}}^a$	2.3	3.0
$F_{1-100 \text{ keV}}^a$	7.4	8.1
$L_{2-10 \text{ keV}}^b$	1.9	4.7
$L_{1-100 \text{ keV}}^b$	6.4	12.7
χ^2/dof	292/241	324/295

^a In units of 10^{-9} erg cm $^{-2}$ s $^{-1}$.

^b In units of 10^{36} erg s $^{-1}$.

1/1000 lower than classical optical depth because of the inclusion of an energy-independent correction term which reduces the Thomson cross-section σ_{T} for photons propagating in the direction of the magnetic field Becker & Wolff (2007, hereafter BW07).

We initially set the radius of the accretion column $r_0 = 0.25$, which corresponds to ~ 1 km for a NS star with mass $M = 1.4M_{\odot}$; the results for the case $\varrho = 0.05$ are reported in Table 6, while in Fig. 7 we show the deconvolved best-fit model and data.

No significant variation is observed in the χ^2 -value when increasing r_0 from 0.25 to 1. A similar statistical result is also obtained assuming $\varrho = 0.2$ ($\chi^2/\text{dof}=294/241$). In this case, a slight decrease is observed both in the electron temperature and optical depth, although their values can be considered unchanged within errors ($kT_e = 6.5^{+8.5}_{-0.8}$ keV and $\tau = 0.29^{+0.11}_{-0.01}$, respectively). The electron temperature drop is not surprising, as in a thermal plus bulk Comptonization scenario the spectral slope and cut-off energy are dictated not only by the plasma temperature and optical depth, but also by the shape of the velocity field and maximum velocity of

Table 7. Absorbed power-law spectral fits of XRT data of IGR J17544–2619.

Spectrum ^a	N_{H}^b	Γ	Flux ^c	L^d	χ^2/dof C-stat (dof) ^e
WT (133–783)	$1.00^{+0.06}_{-0.06}$	$0.69^{+0.04}_{-0.04}$	3.0	4.89	545/570
PC (784–1659)	$1.83^{+0.55}_{-0.49}$	$1.05^{+0.28}_{-0.27}$	0.27	0.46	30/33
PC (4881–7418)	$2.33^{+0.47}_{-0.41}$	$1.39^{+0.25}_{-0.23}$	0.06	0.11	46/42

^a Spectrum (seconds since trigger).^b In units of 10^{22} cm^{-2} .^c Observed 2–10 keV fluxes ($10^{-9} \text{ erg cm}^{-2} \text{ s}^{-1}$).^d 2–10 keV luminosities in units of $10^{36} \text{ erg s}^{-1}$, at 3.6 kpc.^e Cash statistics (C-stat).

the accreting matter (see fig. 4 in F12). Thus, for given (observed) spectral slope and roll-over energy, the higher the values of \bar{Q} , the lower the values of kT_e , as the bulk Comptonization progressively increases its importance at expenses of thermal Comptonization. Even in this case, with $\bar{Q} = 0.2$, the χ^2 remains unchanged for varying r_0 from 0.25 up to 1.

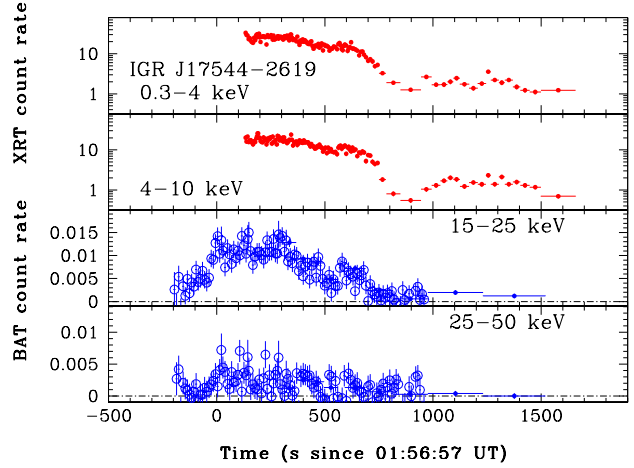
An important issue we want to emphasize is that for XTE J1739–302 the value of τ obtained with COMPAG is less than 1 (see Table 6), and actually the higher the assumed value of \bar{Q} the lower the value of τ .

As the COMPAG model is based on the solution of the Fokker-Planck approximation of the radiative transfer equation, it generally holds for an optical depth $\tau \gtrsim 1$. Our fits on XTE J1739–302 data yield values of τ which are formally smaller than unity. In general terms, this would indicate that the diffusion along the direction of the column axis is not efficient, hence either the spatial diffusion of the photons is only efficient for photons propagating perpendicularly with respect to the column axis, or the system is significantly anisotropic due to the presence of the magnetic field. In either case, the diffusion approximation would not be recommended, as inadequately describing the system (further details can be found in the Appendix).

We note however that, in our case, an acceptable fit can be achieved with a value of the optical depth within a factor of 3 of unity, so that the obtained physical parameters can be discussed with reasonable accuracy. In particular, the electron temperature kT_e results consistent within errors with that obtained with COMPPT and with the hotter BB temperature in the two-BB model (see Tables 4 and 5).

3.2 IGR J17544–2619

The XRT light curve of IGR J17544–2619 is reported in Fig. 2b, and shows the two bright flares observed in the first orbit; the first was caught (WT mode) in the descending part and reached a peak exceeding 50 counts s^{-1} ; the second (PC mode) started off at about $T+750 \text{ s}$ and reached $\sim 5 \text{ counts s}^{-1}$. At about $T+5000 \text{ s}$ (second orbit) the source is still at $\sim 1 \text{ counts s}^{-1}$. Fig. 5 shows the initial data of IGR J17544–2619 in several energy bands. The BAT event-by-event mask-weighted light curves show a slow rise from $T - 200 \text{ s}$ up to the first peak at $T - 0 \text{ s}$, followed by a few more flares, then follows the decaying shape of the XRT light curve. The BAT survey data cover a longer time-span, and show that the source was still detected in the soft band out to $T + 1500 \text{ s}$.

**Figure 5.** Same as Fig. 3 for the 2011 March 24 outburst of IGR J17544–2619. The empty circles correspond to BAT in event mode, filled circles to BAT survey mode data.

We extracted three XRT spectra at different times since the trigger and we fit them with an absorbed power-law model, as detailed in Table 7. The results are summarized in Table 7. By linking the N_{H} across the spectra, we can detect a harder-when-brighter trend and N_{H} variations, as previously observed by Rampy et al. (2009). We note that this is the brightest outburst of this source recorded by *Swift*.

The BAT average spectrum ($T - 239$ to $T+963 \text{ s}$) was fit by a simple power-law model with a photon index $\Gamma = 4.19^{+0.33}_{-0.32}$ ($F_{15-50 \text{ keV}} = 2.4 \times 10^{-9} \text{ erg cm}^{-2} \text{ s}^{-1}$, $\chi^2/\text{dof}=22/20$).

We extracted strictly simultaneous spectra from the XRT and BAT event lists (133–783 s since the BAT trigger; see Fig. 5) and we fit them in the 0.5–10 keV and 15–60 keV energy bands for XRT and BAT, respectively, by adopting the same models as those used for XTE J1739–302. Factors were included in the fitting to allow for normalisation uncertainties between the two instruments, constrained within their usual ranges (0.9–1.1).

As is the case of XTE J1739–302, for IGR J17544–2619 a simple absorbed power-law model is inadequate to fit the broadband spectrum ($\chi^2/\text{dof}=2071/299$). A significant improvement is obtained when considering the CPL and HCP models (Table 3).

The main difference in the χ^2 -values between the CPL and HCP models is due to the residuals of the BAT spectrum above 30 keV, which show in the former case a sinusoidal-like feature in the 15–30 keV region (see Fig. 6). The inclusion of an absorption edge in the CPL model improves the statistical result from $\chi^2/\text{dof}=383/298$ to $\chi^2/\text{dof}=344/296$, with best-fit parameters reported in Table 3. The F-test for discriminating among two different models (namely without and with the absorption edge) provides however a probability of chance improvement (PCI) of about only 20%. The fact that these residuals are not observed in the HCP model besides on fact that in this case the spectrum is less smooth due to the presence of the E_c term. The well constrained determination of the latter parameter is actually indicative for the presence of a change of curvature in the X-ray spectrum around 15–20 keV.

The models WABS × COMPPT yields $\chi^2/\text{dof}=339/297$, and the inclusion of the absorption edge improves the fit to $\chi^2/\text{dof}=323/295$, with however an even lower PCI ($\sim 35\%$) with

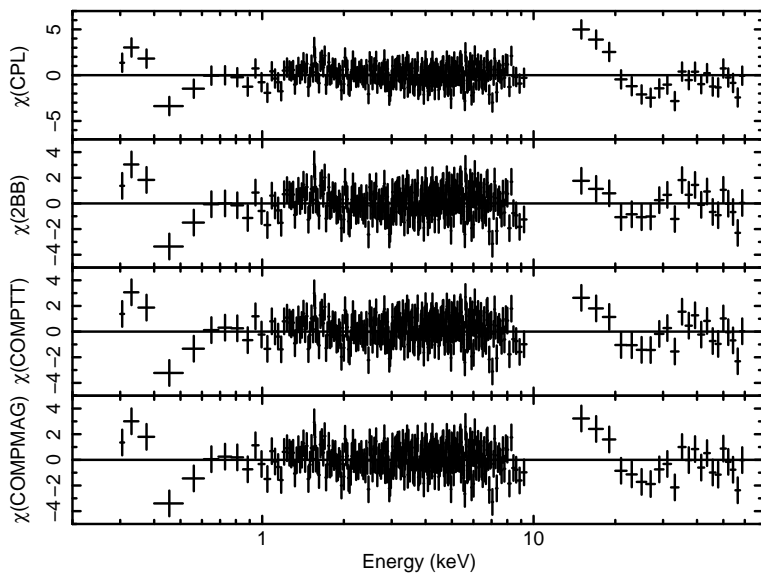


Figure 6. Residuals to data in units of σ of the four models adopted to fit the continuum of IGR J17544–2619 (see Sect. 3.2 for details).

respect to the case of a CPL, and best-fit parameters reported in Table 5.

Similarly to XTE J1739–302, a satisfactory fit can be obtained by the sum of two blackbody spectra (see Table 4), and in this case the inclusion of the absorption edge **only marginally** improves the fit by $\Delta\chi^2 \sim 7$.

Performing the spectral analysis with the COMP MAG model, we followed the same procedure of XTE J1739–302. First, we considered the case of free-fall velocity profile fixing $\dot{Q} = 0.05$, accretion column radius $r_0 = 0.25$ and NS albedo $A = 1$. In this case we obtain $\chi^2/\text{dof}=343/297$, with an improvement $\Delta\chi^2 \sim 20$ when including the absorption edge at 20 keV. Also for IGR J17544–2619, the fit results to be insensitive to r_0 , with the χ^2 -value substantially unchanged for r_0 increasing from 0.25 to 1.

In the second case, namely $\dot{Q} = 0.2$, the inclusion of the absorption edge reduces similarly the fit by $\Delta\chi^2 \sim 20$, but we observed a decreases from $\chi^2/\text{dof}=363/295$ to $\chi^2/\text{dof}=332/295$ by setting $r_0 = 0.25$ and $r_0 = 1$, respectively. For higher values of r_0 , no further improvement of the χ^2 was observed, so that we consider it as our actual best-fit parameter.

Unlike the case of XTE J1739–302, the increased value of \dot{Q} leads to a more significant decrease of the electron temperature, with $kT_e = 1.2^{+0.1}_{-0.1}$ keV, while the optical depth to first approximation remains constant within errors, with $\tau = 1.44^{+0.11}_{-0.09}$.

The reason for this is that a higher value of \dot{Q} is compensated by the simultaneous increase of the accretion column radius r_0 from 0.25 to 1.

In Fig. 6 we report as a summary, the residuals to the data in units of σ of the four different adopted models above described, while Fig. 7 shows the absorption-corrected best-fit models and residuals between the data and the model in units of σ for BBODYRAD+BBODYRAD and EDGE×COMP MAG.

4 DISCUSSION

XTE J1739–302 and IGR J17544–2619 are considered the prototypes of the SFXT class and, as such, were systematically observed

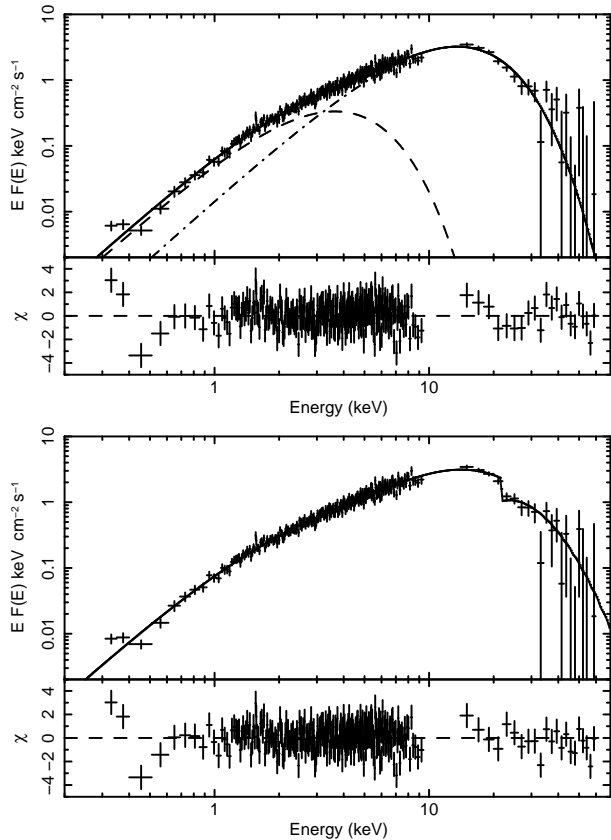


Figure 7. Absorption-corrected $EF(E)$ spectra, best-fit models and residuals between the data and the model in units of σ for IGR J17544–2619. *Upper panel:* BBODYRAD+BBODYRAD. *Lower panel:* EDGE×COMP MAG.

with *Swift*, which caught several outbursts from both sources. The simplest way to parametrise the shape of the broad-band spectra is to fit them with phenomenological models typically used to describe the X-ray emission from accreting pulsars in HMXBs, i.e., absorbed power laws, absorbed power-law models with a high energy cut-offs and absorbed power-law models with exponential cut-offs.

The advantage of this approach is that the fits yield easy-to-compare estimates of fluxes and luminosities for each outburst. Indeed, the data presented in this paper yield values of both high energy cut-off E_c and e-folding energy E_f (see Sect. 3.1 and 3.2) consistent with the ones obtained previously for both sources (Sidoli et al. 2009b,a; Romano et al. 2011c,d, 2010). The disadvantage is, clearly, that little physical insight can be obtained from such fits. In this paper we also apply the following more physically-motivated models: absorbed Comptonization models (COMPTT); a combination of two blackbodies with different temperatures and radii; and for the first time to SFXTs, the new COMP MAG model, recently developed by F12.

There is an interesting aspect to discuss, which has not been yet fully faced in the accretion physics of SFXTs. If we focus on the results using the COMPTT and COMP MAG models, it can be shown that the electron density where Comptonization takes place is of the order of 10^{19} cm^{-3} . Indeed, the Thomson optical depth is given by

$$\tau \approx 7 n_{19} r_6, \quad (1)$$

where $n_{19} \equiv n_e/10^{19}$ and $r_6 \equiv R/10^6$ are dimensionless electron density and system length scale, respectively. If spectral formation

occurs close to the NS ($r_6 \sim 1-2$), from the COMPTT best-fit values of τ reported in Table 5 we obtain $n_{19} \sim 1$.

The possible presence of a strong magnetic field ($B \gtrsim 10^{12}$ G), with associated reduction of the Thomson cross-section σ_T would actually require an even higher electron density, which somewhat compensates the lower cross-section value in order to maintain the same Comptonization parameter Y , and in turn the observed spectral index.

This qualitative effect can be tested from the results of the COMPAG model (Table 6). The electron density for column accretion, which is assumed in COMPAG, is given by

$$n_e \approx 10^{19} \frac{\dot{m}}{mr_0^2 \beta_z} \text{ cm}^{-3}, \quad (2)$$

where $\dot{m} \equiv \dot{M}/\dot{M}_{\text{Edd}}$ is the accretion rate in Eddington units, $m = M_{\text{NS}}/M_{\odot}$ is the NS mass in units of solar masses, $r_0 = R_0/(R_{\odot}^{\text{scw}} m)$ is the accretion column radius in units of the NS Schwarzschild radius, and $\beta_z = V_z/c$ is the accretion column velocity. We derived \dot{m} from the best-fit value of τ reported in Table 6 for IGR J17544–2619 and XTE J1739–302 (with $r_0 = 0.25$ and $\mathcal{Q} = 0.05$) and using equation (44) in F12 for both sources. Then, substituting β_z in equation (2) with a value averaged over the vertical z -coordinate $\langle \beta_z \rangle$, we obtain $n_e \sim 10^{21} \text{ cm}^{-3}$ in both sources, which is actually a factor about one hundred higher than that inferred from COMPTT.

Then, we consider the mass flow rate across the magnetosphere

$$\dot{M} = 4\pi R_m^2 \rho v_{\text{in}}, \quad (3)$$

where R_m is the magnetospheric radius, and v_{in} is the infall velocity at R_m , that is expected to be less than the free-fall velocity

$$v_{\text{ff}} = \left(\frac{2GM_{\text{NS}}}{R} \right)^{1/2}. \quad (4)$$

The accretion luminosity at the NS surface on the other hand is

$$L_{\text{acc}} \lesssim \frac{GM_{\text{NS}} \dot{M}}{R_{\text{NS}}}. \quad (5)$$

Assuming a NS with mass $M = 1.4M_{\odot}$ and radius $R_{\text{NS}} = 10 \text{ km}$, and combining equations (3) and (5) we obtain

$$n_e \gtrsim 1.3 \times 10^{14} \frac{L_{37}}{r_8^2 v_9} \text{ cm}^{-3}, \quad (6)$$

where $L_{37} \equiv L_x/10^{37}$, $r_8 \equiv r_m/10^8$, and $v_9 \equiv v_{\text{in}}/10^9$, respectively.

We consider a magnetospheric radius $r_m \approx 10^8 \text{ cm}$, calculated assuming the typical values of the magnetic field of an accreting pulsar in HMXBs and the typical stellar wind parameters of OB supergiants (Davidson, & Ostriker 1973). Additionally, for the infall velocity we assume for sake of simplicity $v_{\text{in}} \approx v_{\text{ff}}$.

With these prescriptions in mind and noting that both sources during the joint XRT/BAT observation have shown $L_x \lesssim 10^{37} \text{ erg s}^{-1}$, from equation (6) we find that at the magnetospheric radius $n_e \gtrsim 10^{14} \text{ cm}^{-3}$.

This value of the electron density at the magnetospheric radius is about seven orders of magnitude lower than that inferred from the best-fit parameters of COMPAG as shown above, and thus cannot be simply a result of a simplified treatment of the problems such as pure spherical accretion assumed in equation (6).

However, there are at least to issues which are worth mentioning. First, the electron density estimated from the best-fit parameters of COMPAG is related to the region where the X-ray spectral

formation is assumed to take place, which, in the case of COMPAG, correspond to cylindrical accretion column close to the NS surface with characteristic height-scale $H \approx 1-2 R_{\text{NS}}$.

This scale-length is about 1/100 of the assumed magnetospheric radius ($\approx 100R_{\text{NS}}$), and for a density scaling as R^{-2} it would imply to first approximation a density increase from R_m to R_{NS} about $n_e^{\text{NS}}/n_e^m \sim 10^4$. Of course, matter channeling towards the magnetic poles may also play an important role in increasing the matter density in the region close to the NS surface.

The second point to be considered is that if the NS orbital motion is supersonic, strong shock waves are expected to form approximately at the NS magnetosphere (bow shock region). The net result would be thus an increase of the electron density with respect to the value reported in equation (6).

The Mach number of the NS is given by

$$\mathcal{M} \approx 10^2 V_8^{\text{ns}} (\gamma Z T_e / \mu)^{-1/2}, \quad (7)$$

where V_8^{ns} is the NS orbital velocity in units of 10^8 cm s^{-1} , γ is the adiabatic index of the wind, $\mu = m_i/m_p$ its molecular weight, Z its the charge state, and T_e its temperature in eV. For wind temperatures in the range $10^5 - 10^7 \text{ K}$ (Ducci et al. 2009), and velocities of the NS derived from the orbital parameters for both for XTE J1739–302 and IGR J17544–2619, \mathcal{M} varies from a few to about 30, and if the shock is isothermal, $\rho_1/\rho_2 \approx \mathcal{M}^2$. Actually, a density increase of a factor $\sim 10^2$ at the magnetospheric shock front, with respect to the value computed in equation (6), would be sufficient to take into account the electron density derived from COMPAG at the magnetic poles (see above).

The physics of shocks in these systems is however rather complicated for the intrinsic three-dimensional nature of the problem. Indeed, if from one side the supersonic motion of the NS ensures the formation of a bow shock, on the other hand this discontinuity occurs in a region where the presence of a strong magnetic field plays an important role in determining the gas configuration.

A pure dipolar magnetic field may lead to the formation of a bow shock which follows approximately the shape of the magnetic lines in the direction of motion of the NS, together with a channeling of matter towards the magnetic poles. This accretion geometry close to the NS could be approximated with some accuracy by the COMPAG model. However, if non-negligible multipole magnetic field components are present, then matter can also (or mainly) be accreted at the equator of the NS.

As shown in the data analysis, the spectra of both XTE J1739–302 and IGR J17544–2619 can be alternatively described by a two-component model consisting of a soft and hard BB (see Table 4). The temperature of the softer BB is consistent with that of the seed photons in both COMPTT and COMPAG, while the temperature of the harder BB is comparable with the electron temperature of the above mentioned Comptonization models. This means that the harder BB is actually playing the role of a Comptonization feature, but the quality of the high-energy data (see Figs. 4 and 7) does not allow to distinguish between an unsaturated (COMPTT and COMPAG) or saturated (BB) Compton regime.

The apparent radii of both BB components are consistent with emission regions of the order of a polar cap radius, thus pointing in favour of a very compact emission region. The implications for the accretion geometry in this context are that both the regions of the soft seed photons and of the Comptonized ones are visible.

Summarizing, the current data presently do not allow us to distinguish whether the 0.1–60 keV X-ray spectra of XTE J1739–302 and IGR J17544–2619 form as a result of a single unsaturated

Comptonization process, or arise from two different and directly visible zones of seed and Comptonized photons.

Using the calibration of stellar parameters for Galactic O stars of Martins et al. (2005), we find $M_{\text{SG}} \sim 31 M_{\odot}$, $R_{\text{SG}} \sim 21 R_{\odot}$ for XTE J1739–302, and $M_{\text{SG}} \sim 30 M_{\odot}$, $R_{\text{SG}} \sim 22 R_{\odot}$ for IGR J17544–2619, respectively. If the orbital period of XTE J1739–302 is 51.47 d, the minimum and maximum distances of the NS from the giant companion are in the range $d_{\text{min}} \sim 8 - 4.5 R_{\text{SG}}$ and $d_{\text{max}} \sim 9.8 - 13.4 R_{\text{SG}}$ for orbital eccentricity $e = 0.1 - 0.5$, respectively. These values change to $d_{\text{min}} \sim 3.2 - 1.8 R_{\text{SG}}$ and $d_{\text{max}} \sim 3.9 - 5.3 R_{\text{SG}}$ if the orbital period is 12.89 d (see Section 1).

In the case of IGR J17544–2619, on the other hand, the maximum allowed eccentricity for its orbital period of 4.93 d is $e = 0.4$, and the ranges of minimum and maximum distances to the supergiant companion is $d_{\text{min}} \sim 1.6 - 1.1 R_{\text{SG}}$ and $d_{\text{max}} \sim 1.9 - 2.4 R_{\text{SG}}$.

The mass loss rates of the supergiant companions of XTE J1739–302 and IGR J17544–2619 have, within the uncertainties with which we know the masses, radii, effective temperatures and bolometric luminosities of the two stars, the same value of about $2 \times 10^{-6} M_{\odot} \text{ yr}^{-1}$ (Vink et al. 2000).

Whatever the actual orbital period of XTE J1739–302 and the eccentricity of the two systems, the distance to the supergiant companion is lower for IGR J17544–2619. It is thus intriguing to observe that the optical depth derived from the Comptonization models is higher in the latter source than in XTE J1739–302 (see Tables 5 and 6), as one would expect for a closer orbiting system.

5 CONCLUSIONS

We have analyzed data from the outbursts of two sources, XTE J1739–302 and IGR J17544–2619, which are considered to be the prototypes of the SFXTs class. During the bright flare they reached peak luminosities of $\sim 2 \times 10^{36} \text{ erg s}^{-1}$ and $\sim 5 \times 10^{36} \text{ erg s}^{-1}$, respectively.

The presented *Swift* data do not allow us to discriminate whether the X-ray spectra are the result of a single unsaturated Comptonization process, or whether we observe both regions where seed photons are produced and Comptonization mostly takes place (two-BB model).

The electron density in the region of the X-ray spectral formation, computed to first approximation using the best-fit parameters of the COMPAG model, is a factor about 1000 higher than expected from the continuity equation at the magnetospheric radius. We propose that the formation of a bow shock at the NS magnetosphere, due to its supersonic orbital motion around the supergiant companion, may increase the density enough to explain the difference. This effect needs to be investigated in a future work by means of 3D magnetohydrodynamical simulations using the specifically devoted FLASH code.

The possible feature around 20 keV which is observed using a one-component Comptonization model (see Fig. 7, bottom panel) is intriguing, as it can not be attributed to any particular shape of the BAT instrument effective area, however that fact that it is strongly dumped using a two-BB model and it has a low statistical significance do not allow us to draw firm conclusions.

Nevertheless, this feature needs a further investigation with higher-resolution missions in the energy range around 20 keV, in particular with NuSTAR. If true, it would be the first measure ever obtained of the magnetic field intensity ($\sim 2 \times 10^{12} \text{ G}$) in a SFXT.

ACKNOWLEDGMENTS

We thank the *Swift* team duty scientists and science planners, and the remainder of the *Swift* XRT and BAT teams, S. Barthelmy and J.A. Nousek, in particular, for their invaluable help and support of the SFXT project as a whole. We thank C. Guidorzi for helpful discussions. We acknowledge financial contribution from the agreement ASI-INAF I/009/10/0 and from contract ASI-INAF I/004/11/0. PE acknowledges financial support from the Autonomous Region of Sardinia through a research grant under the program PO Sardegna FSE 2007–2013, L.R. 7/2007 “Promoting scientific research and innovation technology in Sardinia”. This work was supported at PSU by NASA contract NAS5-00136.

REFERENCES

- Barthelmy S. D., Barbier L. M., Cummings J. R. et al., 2005, *Space Science Reviews*, 120, 143
- Becker P. A., Wolff M. T., 2007, *ApJ*, 654, 435 (BW07)
- Blay P., Martínez-Núñez S., Negueruela I., et al., 2008, *A&A*, 489, 669
- Bozzo E., Falanga M., Stella L., 2008, *ApJ*, 683, 1031
- Bozzo E., Stella L., Ferrigno C., Giunta A., Falanga M., Campana S., Israel G., Leyder J. C., 2010, *A&A*, 519, A6
- Burrows D. N., Hill J. E., Nousek J. A. et al., 2005, *Space Science Reviews*, 120, 165
- Cash W., 1979, *ApJ*, 228, 939
- Clark D. J., Hill A. B., Bird A. J., McBride V. A., Scaringi S., Dean A. J., 2009, *MNRAS*, 399, L113
- Corbet R. H. D., 1986, *MNRAS*, 220, 1047
- Davidson K., Ostriker J.P., 1973, *ApJ*, 179, 585
- Drave S. P., Bird A. J., Townsend L. J., Hill A. B., McBride V. A., Sguera V., Bazzano A., Clark D. J., 2012, *A&A*, 539, A21
- Drave S. P., Clark D. J., Bird A. J., McBride V. A., Hill A. B., Sguera V., Scaringi S., Bazzano A., 2010, *MNRAS*, 409, 1220
- Ducci L., Sidoli L., Mereghetti S., Paizis A., Romano P., 2009, *MNRAS*, 398, 2152
- Farinelli R., Ceccobello C., Romano P., Titarchuk L., 2012, *A&A*, 538, 67 (F12)
- Grebenev S. A., Lutovinov A. A., Sunyaev R. A., 2003, *Astron. Tel.*, 192
- Grebenev S. A., Rodriguez J., Westergaard N. J., Sunyaev R. A., Oosterbroek T., 2004, *Astron. Tel.*, 252
- Grebenev S. A., Sunyaev R. A., 2007, *Astronomy Letters*, 33, 149
- in’t Zand J., Heise J., Ubertini P., Bazzano A., Markwardt C., 2004, in V. Schoenfelder, G. Lichti, & C. Winkler ed., 5th INTEGRAL Workshop on the INTEGRAL Universe Vol. 552 of ESA Special Publication, A BeppoSAX-WFC Viewpoint of New INTEGRAL Sources, Particularly IGR J17544-2619. p. 427
- in’t Zand J. J. M., 2005, *A&A*, 441, L1
- Israel G. L., Romano P., Mangano V., et al., 2008, *ApJ*, 685, 1114
- Krimm H. A., Barthelmy S. D., Barbier L., et al., 2007, *Astron. Tel.*, 1265
- Kuulkers E., Oneca D. R., Brandt S., et al., 2007, *Astron. Tel.*, 1266
- Martins F., Schaerer D., Hillier D. J., 2005, *A&A*, 436, 1049
- Negueruela I., Smith D. M., Harrison T. E., Torrejón J. M., 2006a, *ApJ*, 638, 982
- Negueruela I., Smith D. M., Reig P., Chaty S., Torrejón J. M., 2006b, *ApJ*, 604, 165
- Negueruela I., Torrejón J. M., Reig P., Ribó M., Smith D. M., 2008, 1010, 252

- Pellizza L. J., Chaty S., Negueruela I., 2006, *A&A*, 455, 653
Rahoui F., Chaty S., Lagage P.-O., Pantin E., 2008, *A&A*, 484, 801
Rampy R. A., Smith D. M., Negueruela I., 2009, *ApJ*, 707, 243
Romano P., Barthelmy S. D., Esposito P., et al., 2011a, *Astron. Tel.*, 3235
Romano P., Esposito P., Evans P. A., et al., 2011b, *Astron. Tel.*, 3182
Romano P., La Parola V., Vercellone S., et al., 2011c, *MNRAS*, 410, 1825
Romano P., Mangano V., Cusumano G., et al., 2011d, *MNRAS*, 412, L30
Romano P., Sidoli L., Cusumano G., et al., 2009, *MNRAS*, 399, 2021
Romano P., Vercellone S., La Parola V., et al., 2010, in *Proceedings of the 25th Texas Symposium on Relativistic Astrophysics*, Online at <http://pos.sissa.it/cgi-bin/reader/conf.cgi?confid=123>, p. 117
Sguera V., Barlow E. J., Bird A. J., et al., 2005, *A&A*, 444, 221
Sguera V., Bazzano A., Bird A. J., et al., 2006, *ApJ*, 646, 452
Sidoli L., Romano P., Ducci L., et al., 2009a, *MNRAS*, 397, 1528
Sidoli L., Romano P., Mangano V., et al., 2009b, *ApJ*, 690, 120
Sidoli L., Romano P., Mereghetti S., Paizis A., Vercellone S., Mangano V., Götz D., 2007, *A&A*, 476, 1307
Smith D. M., Main D., Marshall F., Swank J., Heindl W. A., Leventhal M., in 't Zand J. J. M., Heise J., 1998, *ApJL*, 501, L181
Sunyaev R. A., Grebenev S. A., Lutovinov A. A., Rodriguez J., Mereghetti S., Gotz D., Courvoisier T., 2003, *Astron. Tel.*, 190
Vaughan S., Goad M. R., Beardmore A. P., O'Brien P. T., Osborne J. P., Page K. L., Barthelmy S. D., Burrows D. N., 2006, *ApJ*, 638, 920
Vink J. S., de Koter A., Lamers H. J. G. L. M., 2000, *A&A*, 362, 295
Walter R., Zurita Heras J., 2007, *A&A*, 476, 335

APPENDIX A: THE OPTICAL DEPTH RANGES OF APPLICABILITY OF THE COMPMAG MODEL

The theoretical spectra of the COMPMAG model were reported by F12 for the case of optical depth $\tau < 1$. In this section we better explain how this impacts the spectral fitting analysis of real data. In particular, the fits of the broad-band spectrum of XTE J1739–302 with the COMPMAG model (see Table 6) yield an optical depth formally less than 1, albeit within a factor of 3 from unity. It is worth noting that in COMPMAG this is the vertical optical depth of the accretion column and it is computed including an energy-independent correction to the Thomson cross-section, due to the presence of a magnetic field $B \gtrsim 10^{12}$ G. More specifically, it is the opacity related to photons which diffuse across the field lines. The relation between the optical depth presented in Table 6 can be written in terms of Thomson optical depth as $\tau \approx 10^{-3} \tau_T$, that in the case of XTE J1739–302 is $\tau_T \sim 300$.

After rearranging some terms, equation (35) in F12 can be written as

$$-\frac{\sigma_{\parallel}}{\bar{\sigma}} \mathcal{S}(x, \tau) = -\frac{\sigma_{\parallel}}{\bar{\sigma}} \frac{v}{c} \frac{\partial n}{\partial \tau} + \frac{\sigma_{\parallel}}{\bar{\sigma}} \frac{1}{c} \frac{dv}{d\tau} \frac{x}{3} \frac{\partial n}{\partial x} + \frac{1}{3} \frac{\sigma_{\parallel}}{\bar{\sigma}} \frac{\partial^2 n}{\partial \tau^2} - \left(\frac{\xi v}{c}\right)^2 \frac{\sigma_{\parallel}}{\bar{\sigma}} n + \frac{kT_e}{m_e c^2} \frac{1}{x^2} \frac{\partial}{\partial x} \left\{ x^4 \left[n + \left(1 + \frac{1}{3} \frac{m_e v^2}{kT_e}\right) \frac{\partial n}{\partial x} \right] \right\}.$$

In the escape time prescription provided by BW07, the spatial diffusion of photons is described by

$$\frac{1}{3} \frac{\sigma_{\parallel}}{\bar{\sigma}} \frac{\partial^2 n}{\partial \tau_{\parallel}^2} - \left(\frac{\xi v}{c}\right)^2 \frac{\sigma_{\parallel}}{\bar{\sigma}} n = \lambda^2 n, \quad (\text{A1})$$

or, more clearly, by

$$\frac{1}{3} \frac{\sigma_{\parallel}}{\bar{\sigma}} \frac{\partial^2 n}{\partial \tau_{\parallel}^2} - \frac{n}{r_0 n_e \bar{\sigma} \tau_{\perp}} = \lambda^2 n, \quad (\text{A2})$$

where $d\tau_{\parallel} \equiv d\tau = n_e \sigma_{\parallel} dZ$ is the optical depth along the Z -axis and $d\tau_{\perp} = n_e \sigma_{\perp} dr$ is the optical depth along the r -axis, perpendicular to the magnetic field, and λ is the eigenvalue. The right hand side of equation A2 can be approximated as

$$\left(\frac{10^2}{\tau_T}\right)^2 \left[\frac{1}{3} - \frac{Z_0^2}{10^3 r_0^2} \right] n \approx \lambda^2 n \quad (\text{A3})$$

where $d\tau_T = n_e \sigma_T dZ$ and since the eigenvalue $\lambda^2 < 1$, also the coefficient of n on the right hand side of equation (A3) should be less than 1, in order for diffusion approximation to hold. In particular, the coefficient $\mathcal{D}_{\parallel} = \sigma_{\parallel} / (3\bar{\sigma}\tau_{\parallel}^2)$ takes into account the spatial diffusion of photons propagating along the magnetic field lines, while the coefficient $\mathcal{D}_{\perp} = 1 / (r_0 n_e \bar{\sigma} \tau_{\perp})$ accounts for the diffusion of photon travelling perpendicular to the field.

Following the approach of BW07, from equation (A3) it follows that the diffusion approximation for photons propagating in the direction of the magnetic field is valid if the corresponding Thomson optical depth $\tau_T \gtrsim 10^2$. This can be actually the condition for a meaningful applicability of the COMPMAG model, together with the requirement that both the optical depths τ_{\parallel} and τ_{\perp} need to be larger than unity. From equation (A3) it is also evident that the ratio between the spatial diffusion in the Z -direction (\mathcal{D}_{\parallel}) and in the r -direction (\mathcal{D}_{\perp}) depends upon the choice of the column size (Z_0/r_0).

This paper has been typeset from a $\text{\TeX}/\text{\LaTeX}$ file prepared by the author.